**FMDB** *Transactions on Sustainable Health Science Letters*

# IWPO-Based Attention Convolutional-Modified Inception Network for Classification of Histopathological Breast Cancer

**K. Jayasheel Kumar[1,*], Tarunika Sharma[2], M. Arunadevi Thirumalraj[3], S. Venkatasubramanian[4], Bushra Rehman[5]**

[1]Department of Automobile Engineering, New Horizon College of Engineering, Bengaluru, Karnataka, India.
[2]Department of Applied Sciences, New Horizon College of Engineering, Bengaluru, Karnataka, India.
[3]Department of Computer Science and Engineering, Karunya Institute of Technology and Science, Coimbatore, Tamil Nadu, India.
[3,4]Department of Computer Science and Business Systems, Saranathan College of Engineering, Trichy, Tamil Nadu, India.
[5]Institute of Pathology and Diagnostic Medicine, Khyber Medical University, Peshawar, Khyber Pakhtunkhwa, Pakistan.
jayasheel.81088@gmail.com[1], tarunika.sharma@gmail.com[2], aruna.devi96@gmail.com[3], veeyes@saranathan.ac.in[4], drbushra.ipdm@kmu.edu.pk[5]

**Abstract:** Histopathological images are used to diagnose breast cancer. Interpreting human histopathology images is difficult; hence, AI- and DL-based automated methods are advisable. Characterising the edge region of normal and deformed nuclei and highlighting the structure of small-shaped nuclei are the major challenges. A contourlet-driven attention network (CDAnet) addresses these challenges with a unique attention mechanism and content-preserving sampling. A controlled signal-driven attention system could replace spatial or channel-wise attention. This approach can focus on the nucleus structure boundary or edge information to obtain fine edge details. Contourlet transforms are proposed for managing signal generation. This approach uses wavelets' multi-scale temporal-frequency localisation and strong directionality. Final categorisation is done using the Attention-based Convolutional-Modified Inception Network (AI-UNet). The Improved Wolf package method fine-tunes this network's settings. A convolutional layer with multiple kernel sizes helps the modified inception module learn effective features quickly and efficiently, enabling kernel classification while balancing computation and the presentation of deeper layers. The BCSS model examines segmentation and classifier models using several criteria.

**Keywords:** Histopathological Images; Contourlet-Driven Attention Network; Improved Wolf Package Algorithm; Convolutional-Modified Inception Network; Nuclei Segmentation; AI and DL Techniques.

**Received on:** 02/12/2024, **Revised on:** 10/02/2025, **Accepted on:** 02/04/2025, **Published on:** 07/09/2025

**Journal Homepage:** https://www.fmdbpub.com/user/journals/details/FTSHSL

**DOI:** https://doi.org/10.69888/FTSHSL.2025.000502

**Cite as:** K. J. Kumar, T. Sharma, M. A. Thirumalraj, S. Venkatasubramanian, and B. Rehman, "IWPO-Based Attention Convolutional-Modified Inception Network for Classification of Histopathological Breast Cancer," *FMDB Transactions on Sustainable Health Science Letters*, vol. 3, no. 3, pp. 165–178, 2025.



## 1. Introduction

Among the many major diseases that endanger human life, cancer ranks high on the list of priorities for medical care [1]. Both the number of novel cases and the number of deaths caused by breast cancer appear to have been rising recently. Survival can

*Corresponding author.

be improved with early and accurate diagnosis. While mammograms are the gold standard for early detection, they aren't always accurate, especially when dealing with thick breast tissue, and the radiologist and patient both face risks from X-ray radiation [2]. Expert histopathologists, together with a great deal of time and energy, can diagnose breast cancer. In addition, different histopathologists reach different diagnoses, largely because each has unique prior knowledge [3]. Diagnostic reliability is limited, with an average accuracy of only 75%. Pathologists and other medical professionals use histopathology to study the development of cancer in tissues and organs by carefully examining biopsy samples under a microscope [4]. The structures and cells found in common histopathological specimens are more widely distributed and may be surrounded by different types of tissue at random [5]. It takes time to examine historical photographs physically and to analyse them visually. This calls for knowledge and background. The application of computer-based image analysis is a viable strategy for improving the predictive and analytical capabilities of histopathological images [6]. Even for histopathology pictures, this type of analysis is efficient as it boosts production by providing a trustworthy second opinion for consistent examination. It may take less time to find a problem if this helps. This will reduce the number of fatalities and the workload for pathologists [7]. Text categorisation, picture identification, and object recognition are three areas where machine learning (ML) is now being used effectively. As CAD technology advances, ML is increasingly used to detect breast cancer [8].

Manual feature modelling is required for histopathological image classification using traditional ML algorithms and artificial feature extraction; however, this approach does not require more efficient hardware and offers advantages in terms of computation time [9]. But labelled data are difficult to obtain, and deep learning (DL) applications, especially CNNs, used for histopathology image classification sometimes require many labelled training examples [10]. Even for expert histopathologists, labelling lesions is tedious and time-consuming. Histopathological diagnosis is currently considered the "gold standard" in medicine. By analysing tissue structure, cellular development patterns, and the nucleus and cytoplasm, pathologists can identify the malignant region and the degree of malignancy when examining lesions under a microscope [11]. Staining the tissue allows for easier microscopical study of its constituent parts. Breast lesions can be categorised as either benign or malignant based on their biological activities. Slow, noninvasive growth is characteristic of benign lesions, in contrast to the aggressive metastasis that characterises malignant tumours [12]. Histopathologists have extensive training and experience in medical imaging, yet it remains challenging for them to examine tissue under a microscope and interpret results manually. Histopathological images are complex and diverse owing to subtle variations, cell overlapping, uneven colour distribution, etc., and manual interpretation of such images takes a long time [13]. Second, the histopathologist's expertise, workload, and personal judgment all contribute to making this type of analysis subjective and unreliable. To provide accurate diagnoses, pathologists also require substantial professional training and extensive experience [14]. Consequently, a breast histopathology image classification (BHIC) system capable of distinguishing benign from malignant tissue is critically required. As a result, pathologists will be able to make diagnoses more quickly and easily.

With the rapid advancement of processing power and storage capacity, computer-assisted diagnosis (CAD) software has become an essential tool in the medical industry, particularly for interpreting histopathology images [15]. A CAD system can rapidly pre-classify and filter histopathological images, thereby aiding early diagnosis. As a result, pathologists can devote more time and energy to judgments that require their expert judgment and first-hand expertise, and the process runs more smoothly. Another issue that CAD systems eliminate is the possibility of subjective evaluations [16]. All things considered, this method has high potential for both academic and practical use. In place of channel-level and spatial attention, this paper proposes a multi-scale directional contourlet filter that leverages both the encoder-decoder network's convolutional output transformation and its spatial attention [30]. To zero in on the nucleus cell's border area, the contourlet filter provides additional edge-level information. The direct injection of the contourlet-filtered output into the network eliminates a key problem with deep neural network architecture, the potential loss of crucial edge information [31]. To further ensure that histopathological images retain all their detail and low-frequency components, a wavelet-based pooling approach is used [32]. The combined operation of the suggested technique better preserves the small-sized nucleus found in space. Lastly, AI-UNet performs classification, and its performance is evaluated using publicly available datasets and other metrics. Here is the breakdown of the remaining sections of the paper: Section 2 presents relevant works, Section 3 discusses the suggested model, Section 4 presents the findings and analysis, and Section 5 provides the conclusion [33].

## 2. Related Works

A new lightweight AI model for image categorisation, BCHI-CovNet, was introduced by Addo et al. [17]. Researchers begin by proposing a new multiscale depth-wise separable convolution. To capture patterns at both low and high resolution, a method is introduced that divides input tensors into several tensor fragments, each with a different kernel size. These fragments are then integrated into a single depth-wise convolution [34]. To gather a wealth of second-order statistical data across channels and geographic dimensions, an additional pooling module is added later. This module augments the representation and introduces pixel diversity during training by capturing long-range pixels that contribute significantly to learning using a unique multi-head self-attention method [35]. The resulting features are distinctive and discriminative. These new designs, important for medical devices with limited resources, drastically reduce the computational complexity of model parameters and FLOPs

[36]. Applying the proposed approach to two publicly available datasets, including breast cancer histopathology pictures, yields impressive results. The accuracy values achieved by the suggested method on the BreaKHis dataset are as follows: 99.15% at 40× magnification, 99.08% at 100× magnification, 99.22% at 200× magnification, and 90.87% at 400Ë magnification. Also, using the BACH dataset, it achieves 99.38% accuracy. These findings demonstrate that BCHI-CovNet is highly successful and has great potential for classifying breast cancer histopathology pictures. A complete and interpretable scoring system for the survival risk associated with breast tumour microenvironment morphology was introduced by Amgad et al. [18], as the Histomic Prognostic Signature (HiPS). HiPS measures aspects of epithelial, stromal, immunological, and spatial interaction by correctly mapping cellular and tissue architecture using deep learning. It was built and verified using data from three separate cohorts: tumour stage, nodal status, metastases, or other relevant characteristics. HiPS always outperforms pathologists in predicting survival outcomes.

The stroma and immune system played a significant role in this. Finally, HiPS is a biomarker that has been rigorously tested and verified, helping pathologists and improving patient prognoses. To achieve reliable, precise patch-level retrieval, Tabatabaei et al. [19] used two CBHIR methods, one based on a custom-built dataset. By analysing input pairs with shared histopathological characteristics, the proposed Siamese network may generalise to new images. The suggested CBHIR methods are tested on the top-K accurate Breast (public) and Skin (private) datasets. Finding the sweet spot for K is difficult, and there's a risk that pathologists may be misled by the growing gap between the query and the returned photos as K increases. Based on the author's evaluation of the top first recovered photos, this work is the first of its kind to address this issue on histopathology images. At larger K values, such as 5 and 400, the Breast-twins model outperforms other state-of-the-art methods, achieving the highest F1 score initially. With a 67% improvement in accuracy, skin-twins outperform the newly suggested Convolutional Auto Encoder (CAE). In addition, the Skin-twins model helps pathologists retrieve the top K pictures and their labels by addressing the challenges posed by Spitzoid Tumours of Uncertain. Thus, this method can provide pathologists with a more transparent, trustworthy, and reliable CAD tool, among other benefits. To improve DenseNet's capabilities for picture texture analysis, Yu et al. [20] fused a coordinated attention mechanism. They then built the CA-BreastNet model to categorise microscopic histopathology images of specific breast cancer types in the BreakHis dataset. Crucially, to improve the network's overall accuracy and alleviate accuracy constraints imposed by dataset architectures, convolutional layers are introduced. Our network has high performance, as shown in the linked experimental results, and SECS provides researchers with trustworthy and useful guidance for improving performance [37].

Automatic breast cancer detection is an area that might benefit from our model and method, since convolutional decision trees achieve classification. To acquire effective representations without labels from histopathological medical images using magnification factors, Chhipa et al. [21] have presented a unique self-supervised pre-training technique. Most other recent cutting-edge research has focused on fully supervised learning methods that rely heavily on human annotations. A persistent problem in histopathology, nevertheless, is the dearth of both labelled and unlabeled data. Currently, the field of histopathology has not investigated representation learning without labels. Magnification Prior Contrastive Similarity (MPCS) is a proposed technique that leverages magnification, inductive transfer, and reduced human effort to enable unlabeled self-supervised learning on the BreakHis small-scale breast cancer dataset. Outperforming prior work in fully supervised learning environments across three public breast cancer datasets, including BreakHis, the proposed strategy achieves state-of-the-art performance in malignancy classification with only 20% of labels used for fine-tuning. It also provides preliminary evidence in favour of the idea that additional research is required to confirm that lowering human priority results in supervision. To identify BC in a dataset with exaggeration factors (MF) of 40×, 100×, 200×, and 400×, Al-Jabbar et al. [22] presented two methods, each using two systems. One approach is a combination of convolutional neural network (CNN) models (AlexNet and GoogLeNet) that uses SVM for feature extraction and classification. Consequently, AlexNet + SVM and GoogLeNet + SVM were used to diagnose all BC datasets. The second approach uses artificial neural networks (ANNs) to diagnose all BC datasets. It does this by combining features from convolutional neural networks (CNNs) with fusion features, which are combinations of features derived from fuzzy colour histograms (FCH), local binary patterns (LBPs), and grey-level co-occurrence matrices (GLCMs).

Finally, an ANN was trained to classify the fusion characteristics. When it comes to properly diagnosing BC using histological images (HI), this approach has demonstrated its superiority. With the 400× dataset, the artificial neural network (ANN) technique that uses fusion features achieves 100% success across all measures. Convolutional network-based models have shown promise for the categorisation of breast histopathology images, according to Majumdar et al. [23]. In this study, researchers propose a new rank-based ensemble approach that combines the outputs of three transfer learning CNN models—specifically, GoogleNet, VGG11, and MobileNetV3_Small—rather than relying on a single CNN model. The recommended ensemble model, constructed using the Gamma function, addresses a two-class classification problem using breast histopathology images. Our method outperforms classification accuracy, achieving 96.95% on the ICIAR-2018 dataset and 99.16% at 40X, 100X, 200X, and 400X magnification levels, respectively. Using both single- and multi-magnification histopathology pictures, Taheri and Golrizkhatami [24] have presented two methods for breast cancer diagnosis. The first system proposed uses a DenseNet201 CNN architecture that has already been trained and fine-tuned on the BreakHis dataset. Its job is to identify benign or malignant histological pictures based on certain magnification parameters. The second system

uses only related magnification images for training; it has four subsystems, one for each magnification. The ultimate choice is then made by fusing the findings from these four subsystems. Multiple tests on the BreakHis dataset show that, in every instance, the suggested systems beat the state-of-the-art methods. Nneji et al. [25] proposed automatic learning and classification of breast cancer from histological images using a lightweight separable convolutional network (LWSC). By employing a contrast enhancement technique to extract visually trainable features from histopathology images, the proposed architecture aims to address poor image quality.

To achieve broader receptive fields, the LWSC model employs layers that are coupled in parallel and contain several filters of varying widths. Also included were factorisation and bottleneck convolution layers for dimensionality reduction in models. Compared to conventional convolutional networks, these techniques have greater non-linear expressive capacity while simultaneously reducing computational cost and the number of trainable parameters. The evaluation results demonstrated optimal performance on multi-class categories, with the suggested LWSC model achieving 97.93% specificity. The suggested LWSC achieves results that are competitive with those of other models. Using a hybrid network architecture, SRGAN-ResNeXt, Juhong et al. [26] showed how to train a convolutional network to improve the quality of low-resolution images and to identify individual cells and nuclei in histopathology images stained with hematoxylin and eosin (H&E). This network can help with cancer diagnosis in areas with limited resources. Our network achieved a peak signal-to-noise ratio of more than 30 dB and a structural similarity of 0.93, both of which significantly improve the quality of the resulting images. Compared with outcomes from the popular SRGAN deep-learning approach with bicubic interpolation, the results are clearly better. Furthermore, our model produces high-resolution breast cancer images, which are then segmented using a second bespoke CNN. The segmentation findings for the H&E images have a coefficient of 0.893 and an Intersection over Union of 0.869. Lastly, researchers present the Inception U-net Models and the Jointly Trained SRGAN-ResNeXt Models, which use the pre-trained weights from the separately trained models. There has been encouraging development in the outcomes produced by the jointly trained model. The researchers hope that our bespoke CNNs can alleviate the problem of low-performing microscopes in resource-constrained environments, where access to sophisticated microscopes or whole slide imaging (WSI) systems is limited, preventing the acquisition of high-resolution images.

## 3. Proposed Methodology

### 3.1. BCSS Dataset

The Breast Cancer dataset includes ground-truth masks and 151 whole-slide images stained with H&E, corresponding to 151 histologically confirmed breast cancer cases. The medical practitioner who oversaw the study and obtained the top pathologist's approval chose a representative ROI for each slide. The regions of interest (ROIs) were chosen to reflect the most common types of regions and textures on each slide. The five tissue types in the BCSS dataset are tumour, stroma, inflammatory infiltration, necrosis, and other categories. Researchers used the remaining photos for training and selected slides from seven universities to form our test set. For the training sets, researchers used data augmentation techniques, including shifts and crops, as well as random horizontal and vertical flips. As a final step, the training and testing sets were each provided with 512×512-pixel tiles containing 3154 and 1222 pixels, respectively. To reduce misalignment across classes, researchers employed a weighted categorical cross-entropy loss, where the relative importance of each class was established by $W_c = 1 - \frac{N_c}{N}$, where N is the sum of pixels in the training dataset and $N_c$ is the sum of pixels going to class c.

### 3.2. Segmentation Using CDNetwork

The authors of this study present CDAnet, a contourlet-driven attention network that incorporates directional, multi-resolution signals to enrich the network with fine-scale detail. In this suggested technique, which has an encoding and a decoding component, the baseline network is based on a standard U-Net-like architecture. Two distinct changes are implemented in this conventional encoder-decoder design:

- Using spatial-level information derived from the conventional U-net design, the goal is to incorporate multi-level directional features. The goal of this method is to improve the model's ability to capture the nuclear structure's fading border region by augmenting spatial information. The goal of using the contourlet transform to generate an edge-aware transformed signal is to achieve this. Nevertheless, researchers suggest a different approach that uses spatial-domain information at various levels of the encoder-decoder architecture as input to the network. The images serve as a control signal that helps the model zero in on the edge region and, ultimately, capture the network's edge details.
- Objects in a small spatial domain are particularly vulnerable to the unintended consequences of the network's spatial downsampling step. This approach uses wavelet pooling rather than the more conventional max or average pooling because the wavelet transform preserves the image's original texture within a narrow spatial region.

### 3.2.1. Wavelet-Based Pooling Strategy

The backbone network resembles U-net topologies in that it is an encoder-decoder network. Instead of the usual up-and-down-sampling process in the section, the 2D sampling technique is used. The downsampling technique is often implemented in popular encoder-decoder architectures such as U-Net and Unet++ using max or average pooling. Aliasing occurs when several data frequency components of a signal are downsampled without accounting for the Nyquist sampling theorem. Therefore, these techniques may erase some data. In contrast, max-unpooling and bilinear interpolation are commonly employed for up-sampling operations in the decoder section. While they can be used to retrieve some data, it is impossible to reconstruct it in its entirety. By preserving the spectral content in the encoder unit and restoring the original content with minimal loss in the decoder, a wavelet-based sampling technique can address this difficulty. A series of processes is initially applied to the input picture. Then, the DWT and IDWT procedures replace downsampling and upsampling at each level of the encoder and decoder, respectively. Here is how the DWT breaks down the signal: three parts at high frequencies and one part at low frequencies:

$$X_{ij} = \left(f_{ij} * X\right) \downarrow 2 \quad (1)$$

where $(.)_{\downarrow 2}$ stands for the two processes, $f_{ij}$ characterises the filters (low-pass and high-pass) to be used, and * indicates that the operation will be convolution. The subscript indicates the filtered output. $X_{ij}$ and three high-pass filters are represented by lh, hl, and hh, whereas ll stands for a low-pass filter. By mixing the high-frequency components with the decoding stage's outputs and then transmitting the subsequent layers, the feature map can be recovered using an IDWT operation:

$$X = \sum f_{ij} * X_{\uparrow 2} \quad (2)$$

Here, $(.)_{\uparrow 2}$ characterises the 2 times upsampling process.

### 3.2.2. Contourlet Driven Attention Mechanism (ConDAM)

In edge regions where picture quality is not significant, using the DWT process instead of max or average pooling in construction may not always prevent information loss. It can make the segmentation process less efficient and introduce unnecessary noise. A controlling signal that carries edge-aware information in multiple directions is needed to drive an attention mechanism that delivers network-level information at the edge. In this work, researchers propose a contourlet-transform-driven attention method to achieve this goal. In the parts that follow, you can see the suggested attention mechanism in action.

#### 3.2.2.1. Controlling Signal

When extracting useful information from two-dimensional images, the contourlet allows for a flexible realisation of multi-resolution and directional decomposition [27].

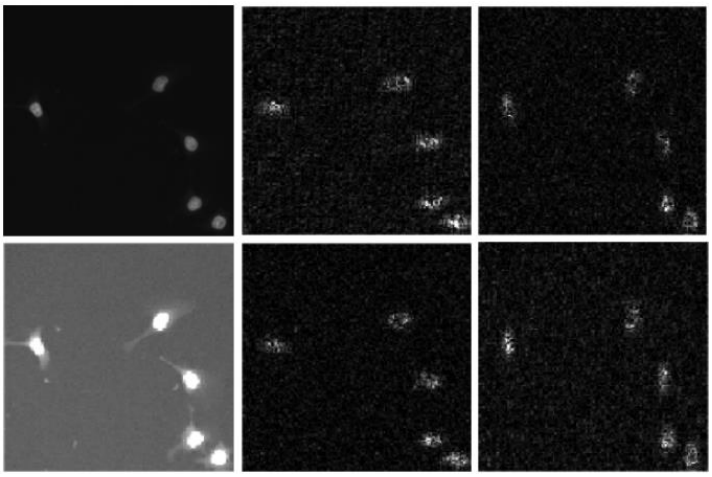

**Figure 1:** The histopathological image is transformed using the contourlet algorithm, where it is first decomposed into one scale and then subdivided into four directional bands, for clarity of presentation, coefficients with smaller values are shown in black, while larger coefficients are shown in white

It excels at describing the picture's most important features—edges, lines, curves, and contours—making it a good fit for

multiscale edge-based image analysis. Two distinct filtering methods make up the contourlet process. An image's multi-resolution features may be extracted using a Laplacian pyramid filter, and the picture can be decomposed into its parts using directional filter banks. Conventional contourlet filter architecture using directional filter bank (DFB) and Laplacian pyramid (LP). A low-pass-filtered, coarser image—the detail image—is first produced by the Laplacian Pyramid level. The next step is to apply the DFB to the detailed picture to obtain the edge signal's directional information. DFB results in 2^l frequency partitioning and is essentially an l-level binary decomposition of a signal. As seen in Figure 1, our approach uses decomposition, yielding one coarser picture and four components of band-pass-filtered directional images.

### 3.2.2.2. Driven Attention Module

Researchers propose an attention technique that integrates the semantics of image data. At first, the controlling signal is formed by concatenating the directional components from the operation. A 1 × 1 convolutional operation follows this. As an alternative, a 1 × 1 convolutional block is used to linearly transform the decoder-level information and feed it into our attention block. A new feature map M is generated by multiplying the resulting control and input signals and passing the result through a SoftMax activation function. The control signal's probability distribution is generated using the SoftMax procedure. The significant areas obtained from the controlling signal are extracted by further multiplying the resulting feature map with the convoluted controlling signal (SC). The subsequent equation provides a concise summary of the entire process:

$$S_O = \text{Softmax}(\phi_1(X)\phi_2(S)^T)\phi_2(S) \quad (3)$$

Here, $\phi_1$ and $\phi_2$ is the 1 × 1 process of convolution. To avoid information overload, a gating mechanism is now being considered to control the amount of incoming signal augmentation. G, the gating mechanism, is made up of a linear layer and a sigmoid activation function. The following is one way to depict the final feature map ϕ_att that is created by the gating mechanism:

$$\phi_{att} = G.X + (1 - G).S_O \quad (4)$$

The following equation defines a network, which is a typical binary cross-entropy loss, as the problem is a problem:

$$\mathcal{L} = \frac{1}{N}\sum_{j=1}^{N} p_j \log y_j + (1 - p_j) \log(1 - y_j) \quad (5)$$

where $p_j$ represents the foretold likelihood value of the jth sample, $y_j$ signifies the consistent label, and N is the overall number of tasters.

### 3.3. Classification Using AI-UNet

Figure 2 depicts the architecture of the AI-UNet. Using a deep, -shaped structure, the network's overall design is comparable to a standard U-net.

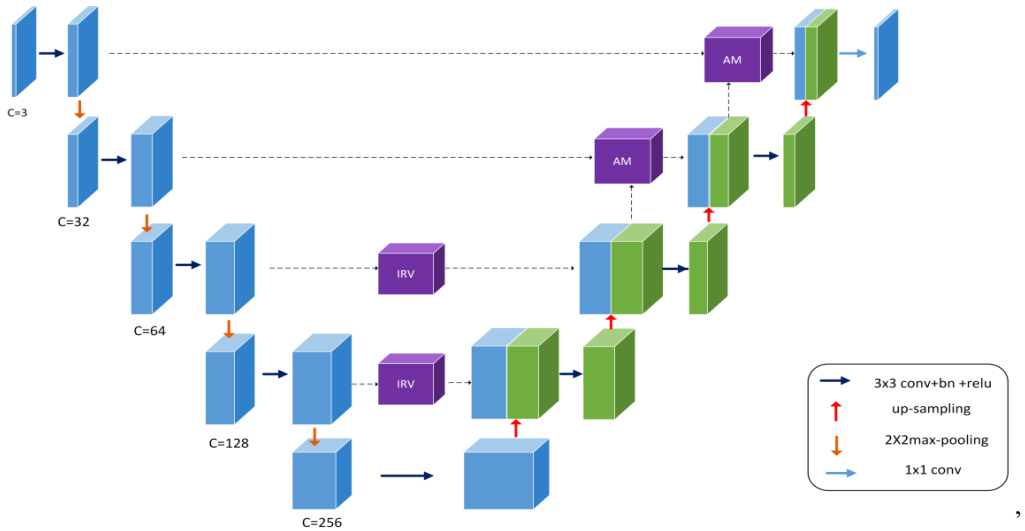


**Figure 2:** Overview of the future AI-Unet construction

To achieve flexible feature extraction and balanced network usage, the study employs varying kernel sizes in both deep and shallow layers. Two inception modules are used to extract deep semantic information from the three-channel input image with greater accuracy during downsampling. Afterwards, the image is processed by three separate convolutional modules. Compared to the traditional U-Net, the total number of channels used in the encoding stage is cut in half, and the image size is reduced by half after each downsampling. To fit the 5x split picture size, researchers cropped the original shot during pre-processing. After upsampling and restoring the picture resolution via bilinear interpolation, the feature maps generated during encoding were skip-connected. Before the final two skip connections, the feature map learns to attend. It lessens the number of duplicate jump connections and prevents redundant information from being triggered during the step. A single-channel grayscale map is obtained by downscaling the final feature map.

### 3.3.1. Convolution Stage

Each convolutional module has four activation functions available: convolution, batch normalisation, dropout, and leakyrelu. Choose a kernel scope of 3 x 3, a stride of 1, and filling of 1 as parameters. A value of 0.3 is chosen for the dropout parameter. Neurons can continue receiving information even after the ReLU function enters the negative range due to the leaky ReLU. The dropout helps mitigate overfitting.

### 3.3.2. Modified Inception Stage

Dimensional convolution and supervision using convolution kernels of varying sizes and channel densities were introduced by Szegedy et al. [28]. The settings, including filter combinations and pooling layers, are determined by the network itself. To build a bottleneck layer, decrease computation, shrink network channels, and increase, a 1x1 is used. The representation size can be greatly reduced without affecting network performance, and significant computational savings can be achieved by implementing a well-designed bottleneck layer. In Figure 3, the inception process highlights how optimising network performance is helped by varying kernel sizes and network breadth. For a broader perspective and to extract more abstract information, large convolutional kernels are the way to go. In contrast, tiny convolution kernels are the way to go for pinpoint pixel identification. To boost scalability and expand the network's reach, the module runs three operations simultaneously. Part one involves using a residual concept to reduce network overfitting. After dimensionality reduction, in the second step, researchers extract linear features and a 5 × 5 feature using convolution. After that, configure the bottleneck layer and dropout settings as needed. Part three involves dividing the 5 × 5 kernel into 1 × 5 and 5 × 1 pieces. The original cuts the computing cost by 1/25.

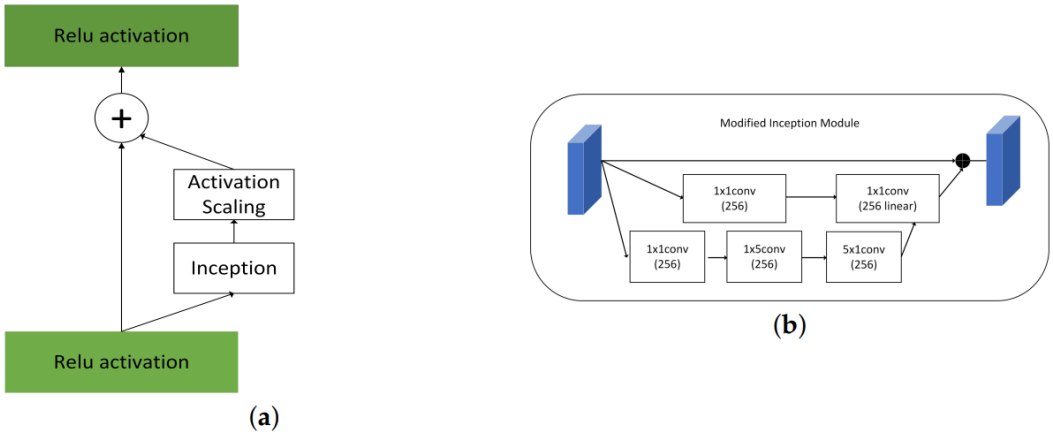


**Figure 3:** (a) Inception (b) changed inception unit

### 3.3.3. Attention Stage

The attention mechanism focuses on important details while ignoring background noise. The two characteristics are later fused using the unit shown in Figure 4. In histopathology photos, where even a minor chin can cause the loss of minor cell nuclei around the figure's edges, this attention structure extracts fine details from the image. To create a gating sign that reflects the importance of features at different spatial positions, researchers must first modify the encoding's output features before concatenation. Integration of encoder-extracted features with decoder-generated feature maps following upsampling, maintaining precision. Next, a 1 × 1 convolution is used to reduce the feature map, introducing nonlinearity and making the channels more relevant. Relu introduces nonlinearity. Based on the proportion of pixels belonging to the nucleus, the sigmoid transforms the feature map values to the range 0 to 1, which in turn assigns weights to the nucleus pixel values at different locations. Lastly, a map of attention features is obtained. One important aspect is to prioritise the foreground, or nucleus, by using a feature map with stronger semantic properties to weight the current feature map.

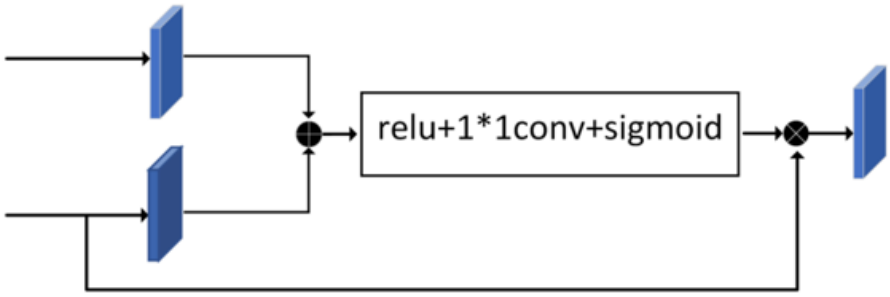


**Figure 4:** Attention module

### 3.4. Fine-Tuning of the Proposed Model Using the IWPA Model

The social distribution of work is evident in wolves, who are gregarious animals—the wolf pack benefits from both its individual and collective efforts to ensure its continued existence and growth. A search route construction method based on task and topic division is the Wolf Pack Algorithm (WPA). Wandering, calling, siege, and updating processes make up the bulk of WPA.

#### 3.4.1. Walk Behaviour

Wolf packs approach their prey from all directions based on their keen sense of smell. Every wolf's fitness level is determined independently. The wolf assumes the role of leader and resumes calling if the search effort exceeds its fitness level. One way to look at this tendency is as the WPA's capacity for global development:

$$x_{id}^{p} = x_{id} + \sin\left(2\pi \times \frac{p}{h}\right) \times step_{s}^{d} \quad (6)$$

$x_{id}^{p}$ is the spatial site of the scout wolf ; $step_{s}^{d}$ is the phase distance of the scout, p is the sum of nominated examination instructions.

#### 3.4.2. Call Behaviour

Once the resting phase is over, the dominant wolf will summon its furious counterpart, who will then swiftly bring the other wolves in the area to its location. The aggressive wolf will then look for prey after sprinting to catch up to its leader. As the assault progresses, the furious wolf will eventually become the head wolf if its fitness level is high enough. The aggressive wolf changes into a siege mode when the distance between it and its leader drops below a certain threshold:

$$x_{id}^{k+1} = x_{id}^{k} + step_{b}^{d} \times \frac{g_{d}^{k} - x_{jd}^{k}}{\left|g_{d}^{k} - x_{jd}^{k}\right|} \quad (7)$$

$x_{id}^{k+1}$ is the spatial site of the violent wolf ; $step_{b}^{d}$ is the attack pace length ; $g_{d}^{k}$ is the wolf.

#### 3.4.3. Siege Behaviour

The local search capabilities of WPA might be likened to the vicious wolves and scouts working together to imprison it:

$$x_{id}^{k+1} = x_{id}^{k} + \lambda \times step_{w}^{d} \times \left|G_{d}^{k} - x_{id}^{k}\right| \quad (8)$$

Where λ characterises the random sum among [-1,1]; $step_{w}^{d}$ is the attack step ; $G_{d}^{k}$ is the spatial site of the prey. Among them, $step_{s}^{d}$, $step_{b}^{d}$, $step_{w}^{d}$ the step length association of the three is:

$$step_{s}^{d} = \frac{step_{b}^{d}}{2} = 2 \times step_{w}^{d} = \frac{|M_{d} - m_{d}|}{C} \quad (9)$$

The C in the formulation is the phase size factor.

### 3.4.4. Upgraded WPA Based on the Genetic Procedure

The principles of survival of the fittest" and "natural selection" are the basis of GA. This program mimics the natural selection process by searching randomly. Selection, crossover, and variation are the three primary components of GA. N individuals were generated at random as the starting population A, with the following parameters: the maximum number of generations, T; the population size, N; the cross likelihood, P; and the variation likelihood, S:

- **Select:** Members of the group who have adapted well. You may use these chosen people to start a new generation. Generations of populations are created by drawing a subset of the present population. Each person's fitness level is used to calculate their selection likelihood.
- **Cross connection:** Genes from two separate individuals that are located at the same place are exchanged to create new individuals in the following generation that are selected for reproduction.
- **Heteromorphosis:** Affected individuals should have certain genes altered. A more diverse population is less likely to fall into local optima. Keep going until either the specified goal value or the maximum sum of iterations is attained, as indicated by the requirements being satisfied.

### 3.4.5. Improve the Binding Apparatus of WPA

This work aims to increase optimisation speed by endowing the population with genetic features and updating wolves' locations adaptively in a stepwise manner. It also discusses the GA behaviour. By combining GA with WPA, researchers can boost the algorithm's global search capability and convergence speed while enhancing WPA's performance. Using WPA and GA as comparisons, this research finds that 100 iterations is the upper limit for both methods. Researchers have specified the following settings for WPA: N=100, a=0.5, S=20, T=20, and D=10 for the distance-determination factor, step length, number of walk orientations, and artificial wolf scale, respectively. Ch=2 is the chromosomal length, Se=0.4 is the selection probability, Cr=0.7 is the crossover likelihood, mu=0.3 is the variation probability, and M=100 is the maximum sum of iterations for the GA. Table 1 shows the results of comparing the three algorithms' performance.

**Table 1:** Comparison of each procedure

| | The optimal sum of repetitions is reached | Actual least distance | Ideal least distance |
|---|---|---|---|
| **WPA** | 43 | 149.4355 | 140.0071 |
| **GA** | 50 | 150.2711 | 140.0071 |
| **The improved WPA** | 25 | 140.3194 | 140.0071 |

## 4. Results and Discussion

The models are trained on a single NVIDIA RTX 8000 GPU using the optimiser. The initial learning rate is set to 0.001 and adjusted according to the 1-cycle learning rate policy.

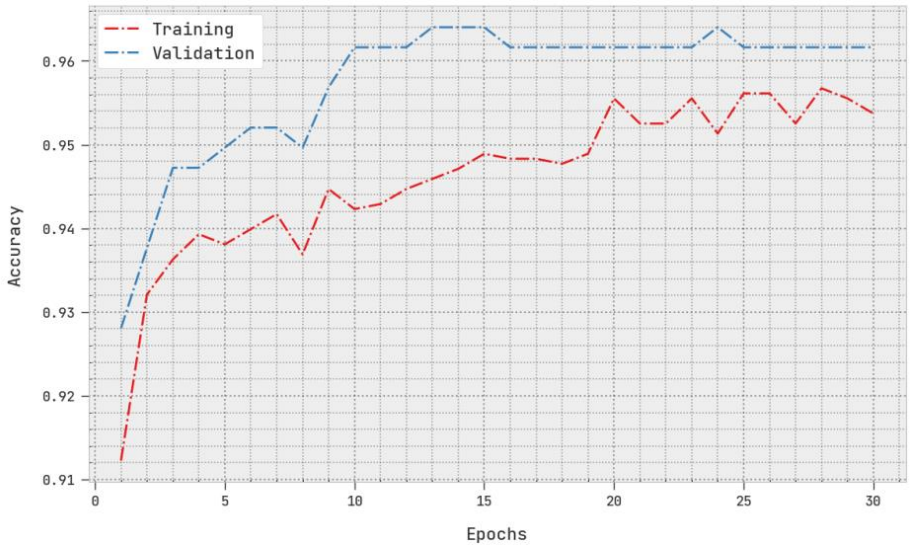


**Figure 5:** TACC and VACC analysis of the proposed model

The representations are applied in Rashmi et al. [29]. Figures 5 and 6 show the accuracy and loss of the suggested model.

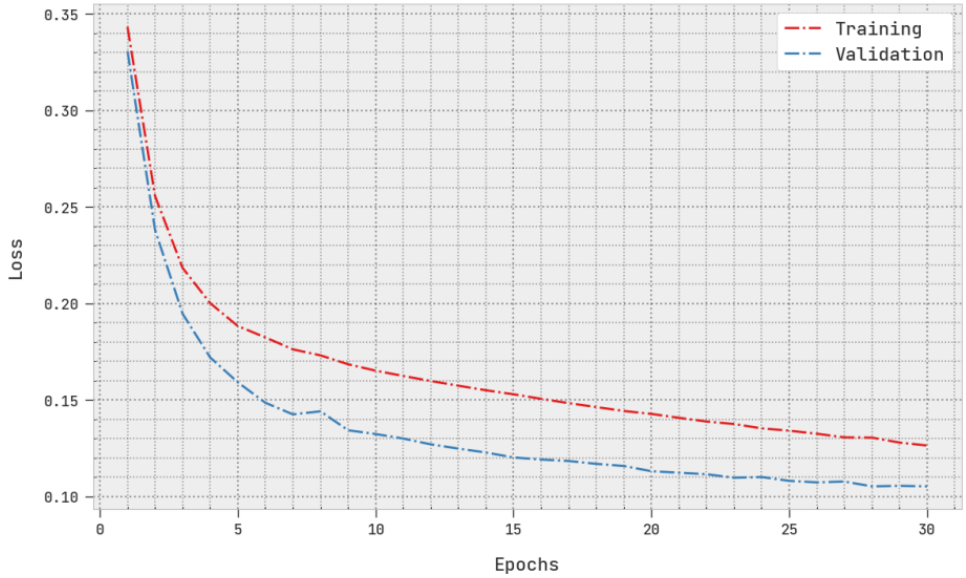


**Figure 6:** Loss of the proposed model on the training and validation datasets

### 4.1. Analysis of Segmentation Results

Table 2 presents the segmented values of the projected perfect with existing procedures across numerous metrics.

**Table 2:** Analysis of various segmented models

| Model | DSC | IOU | Pre | Re | Acc | F1 |
|---|---|---|---|---|---|---|
| FCM | 0.834 | 0.791 | 0.803 | 0.827 | 0.867 | 0.871 |
| ARKFCM | 0.920 | 0.906 | 0.904 | 0.872 | 0.895 | 0.910 |
| Otsu Thresholding | 0.924 | 0.919 | 0.926 | 0.885 | 0.901 | 0.914 |
| K-Means | 0.928 | 0.914 | 0.907 | 0.911 | 0.947 | 0.932 |
| Attention | 0.946 | 0.920 | 0.941 | 0.938 | 0.926 | 0.943 |
| CDANet | 0.967 | 0.924 | 0.968 | 0.951 | 0.996 | 0.959 |

In Table 2, the Analysis of various segmented models. In the analysis of the FCM model, the DSC of 0.834, IOU of 0.791, precision of 0.803, recall of 0.827, and accuracy of 0.867, and f1-score of 0.871 correspondingly. Then the ARKFCM model attained DSC of 0.920, IOU of 0.906, precision of 0.904, accuracy of 0.895, and f1-score of 0.910. Then the Otsu Thresholding model attained DSC of 0.924, IOU of 0.919, precision of 0.926, recall of 0.885, accuracy of 0.901, and f1-score of 0.914. Then the Means model attained DSC of 0.928, IOU of 0.914, precision and recall of 0.911, accuracy of 0.947, and f1-score of 0.932. Then the Attention model attained DSC of 0.946, IOU of 0.920, precision of 0.941, recall of 0.938, accuracy of 0.926, and f1-score of 0.943. Then the CDAnet model attained DSC of 0.967, IOU of 0.924, precision of 0.968, recall of 0.951, accuracy of 0.996, and f1-score of 0.959.

### 4.2. Analysis of Classification Results

Here, classification is performed using 5-fold and 10-fold cross-validation, as shown in Tables 3 and 4.

**Table 3:** Validation analysis of the projected model for 5-fold

| Metric | Accuracy | Precision | Recall | F1-Score | CPU Time | Model (MB) |
|---|---|---|---|---|---|---|
| AI-UNet - IWPOA | 0.97986 | 0.94868 | 0.98084 | 0.96383 | 7 min 53 s | 1.22 |
| AI-UNet | 0.76594 | 0.61794 | 0.89682 | 0.63602 | 31 min 41 s | 0.03 |
| DenseNet | 0.83418 | 0.75511 | 0.92699 | 0.76773 | 30 min 6 s | 7.69 |

| | | | | | | |
|---|---|---|---|---|---|---|
| DarkNet | 0.87806 | 0.78463 | 0.93476 | 0.83175 | 29 min 50 s | 7.69 |
| AlexNet | 0.87147 | 0.77572 | 0.94066 | 0.8257 | 27 min 3 s | 1.62 |
| VGGNet | 0.94099 | 0.93122 | 0.93127 | 0.91357 | 29 min 31 s | 350.73 |
| ResNet | 0.9425 | 0.9656 | 0.9635 | 0.90961 | 28 min 7 s | 29.60 |
| LeNet | 0.90922 | 0.88756 | 0.8952 | 0.8906 | 33.43 s | 35.19 |

The above Table 3 signifies that the Validation Analysis of the projected model for a 5-fold. In the analysis of the AI-UNet – IWPOA model, the accuracy is 0.97986, the precision is 0.94868, the recall is 0.98084, the f1-score is 0.96383, the CPU time is 7 min 53 s, and the model size (MB) is 1.22. Then the AI-UNet model reached the accuracy of 0.61794 and CPU time of 0.89682, and CPU time 31 min 41 s, and model (MB) of 0.03 correspondingly. Then the DenseNet model reached an accuracy of 0.83418, a precision of 30 min 6 s, and a CPU time of 7.69, respectively. Then the DarkNet model reached the accuracy of 0.87806 and precision as 0.78463, 0.93476, and CPU time as 0.83175, and CPU time as 29 min 50 s and model (MB) of 7.69 correspondingly. Then the AlexNet model reached the accuracy of 0.87147 and precision 0.8257, 27 min 3 s, and model (MB) of 1.62 correspondingly. Then the VGGNet model reached an accuracy of 0.94099, precision of 0.93127, CPU time of 0.91357, and model (MB) of 29 min 31 s and model (MB) of 350.73, correspondingly. Then the ResNet model reached an accuracy of 0.9425, a precision of 0.9656, a recall of 0.9635, a CPU time of 28 min 7 s, and a model size (MB) of 29.60. Then the LeNet model reached an accuracy of 0.90922 and a precision of 0.88756, with model (MB) of 33.43 s 3 and model (MB) of 5.19, respectively. Table 3 represents the Validation Analysis of the projected model for a 5-fold.

**Table 4:** Experiments of the proposed model for 10-fold analysis

| Metric | Accuracy | Precision | Recall | F1-Score | CPU Time | Model Size (MB) |
|---|---|---|---|---|---|---|
| AI-UNet - IWPOA | 0.9518 | 0.9538 | 0.9284 | 0.9403 | 21.6 s | 23.6 |
| AI-UNet | 0.9083 | 0.9036 | 0.8869 | 0.8947 | 3.29 s | 13.6 |
| DenseNet | 0.9323 | 0.4665 | 0.4739 | 0.4690 | 36.1 s | 1.8 |
| DarkNet | 0.7539 | 0.3031 | 0.2942 | 0.2850 | 31.5 s | 0.005 |
| AlexNet | 0.8308 | 0.3308 | 0.4789 | 0.3701 | 13 min 48 s | 0.027 |
| VGGNet | 0.7701 | 0.4887 | 0.3476 | 0.3682 | 11 min 10 s | 7.7 |
| ResNet | 0.8536 | 0.6058 | 0.4518 | 0.4902 | 11 min 1 s | 7.7 |
| LeNet | 0.8682 | 0.9189 | 0.7632 | 0.8013 | 10 min 50 s | 1.6 |

Table 4 above presents the experiments for the proposed model's 10-fold cross-validation. In the analysis of the AI-UNet - IWPOA model, the accuracy is 0.9518, the precision is 0.9538, the recall is 0.9284, and the f1-score is 0.9403. The CPU time is 21.6 s, and the model size (MB) is 23.6, respectively. Then the AI-UNet model reached an accuracy of 0.9083, a precision of 0.9036, a CPU time of 3.29 s, and a model size (MB) of 13.6. Then the DenseNet: 0.9323, precision: 0.4665, recall: 0.4739, model size (MB): 0.4690, 36.1s, and model size (MB): 1.8 correspondingly. Then the DarkNet model reached an accuracy of 0.7539, CPU time of 0.3031, model size (MB) of 0.2942, model size (MB) of 0.2850, CPU time of 31.5 s, and model size (MB) of 0.005, correspondingly. Then the AlexNet model reached an accuracy of 0.8308, a precision of 0.3308, a recall of 0.4789, a CPU time of 0.3701, a CPU time of 13 min 48 s, and a model size (MB) of 0.027. Then the VGGNet model reached an accuracy of 0.7701, a precision of 0.4887, a recall of 0.3476, a CPU time of 0.368211 min 10 s, and a model size (MB) of 7.7. Then the ResNet model reached an accuracy of 0.8536, a precision of 0.6058, a recall of 0.4518, a CPU time of 0.490211 minutes, and a model size (MB) of 7.7. Then the LeNet model reached an accuracy of 0.8682, precision of 0.9189, recall of 0.8013, CPU time of 10 min 50 s, and model size (MB) of 7632; then, with a model size (MB) of 1.6, it reached an accuracy of 0.8682, precision of 0.9189, recall of 0.8013, CPU time of 10 min 50 s, and model size (MB) of 1.6.

## 5. Conclusion

Clinicians can benefit from comprehensive information extracted through segmentation, which helps them focus on specific areas of interest and make an accurate diagnosis. This study proposes CDANet, a deep neural network architecture that leverages contourlet-driven attention to separate nuclei in histopathology pictures. Two important problems with nuclear properties are addressed by the proposed design. The first one is the area with few nuclei, while the second one is the area with fuzzy edges. Because they both lie in a low-dimensional space that may be omitted during segmentation, they pose tricky scenarios. For breast cancer classification using histopathology images, a modified U-Net, AI-UNet, is proposed. The model accomplished this by modifying a standard U-Net with an attention and inception module, increasing the total number of channels, and adjusting the number of inputs. For example, when dividing separate nuclei at the periphery of tightly packed cells, the attention module can focus on smaller targets. The inception module can significantly broaden the receptive field. In general, the network architecture can extract basic information from lower layers and more sophisticated semantic information

from deeper layers. An attention apparatus is employed to bolster the feature fusion component of the decoding process. Using IWPOA on the parameters of the future model improves classification accuracy. Researchers want to make full use of data from the nuclear border and mass in our future efforts, particularly for overlapping or poorly defined nuclei. In addition to improving generalizability, the new network architecture will make it applicable to a wider variety of pathological medical datasets. To efficiently complete basic binary classification tasks, models use fewer parameters and fewer iterations.

**Acknowledgement:** The authors express their sincere gratitude to New Horizon College of Engineering, Karunya Institute of Technology and Science, Saranathan College of Engineering, and Khyber Medical University for their continuous support throughout the research work.

**Data Availability Statement:** The data that support the findings of this study are available on request from the corresponding author.

**Funding Statement:** This study and manuscript were conducted without any external funding, institutional support, or sponsorship of any kind.

**Conflicts of Interest Statement:** The authors confirm that there are no known financial or personal conflicts of interest that could have influenced the outcomes or interpretation of this research.

**Ethics and Consent Statement:** This study was conducted in strict accordance with approved ethical guidelines and received clearance from the institutional review boards of all participating institutions. Informed consent was obtained from every participant before their involvement in the study.

**References**

1. H. Hu, S. Qiao, Y. Hao, Y. Bai, R. Cheng, W. Zhang, and G. Zhang, "Breast cancer histopathological images recognition based on two-stage nuclei segmentation strategy," *PLOS ONE,* vol. 17, no. 4, pp. 1–26, 2022.
2. R. Kashyap, "Breast cancer histopathological image classification using stochastic dilated residual ghost model," *Int. J. Inf. Retr. Res. (IJIRR),* vol. 12, no. 1, pp. 1–24, 2022.
3. Y. Zhao, J. Zhang, D. Hu, H. Qu, Y. Tian, and X. Cui, "Application of deep learning in histopathology images of breast cancer: A review," *Micromachines,* vol. 13, no. 12, pp. 1–30, 2022.
4. A. H. Hassan, M. E. Wahed, M. S. Metwally, and M. A. Atiea, "A hybrid approach for classification breast cancer histopathology images," *Front. Sci. Res. Technol.,* vol. 3, no. 1, pp. 1–10, 2022.
5. V. K. Reshma, N. Arya, S. S. Ahmad, I. Wattar, S. Mekala, S. Joshi, and D. Krah, "Detection of breast cancer using histopathological image classification dataset with deep learning techniques," *BioMed Res. Int.,* vol. 2022, no. 1, pp. 1–14, 2022.
6. M. A. Khalil, Y. C. Lee, H. C. Lien, Y. M. Jeng, and C. W. Wang, "Fast segmentation of metastatic foci in H&E whole-slide images for breast cancer diagnosis," *Diagnostics,* vol. 12, no. 4, pp. 1–16, 2022.
7. X. Zhang, X. Zhu, K. Tang, Y. Zhao, Z. Lu, and Q. Feng, "DDTNet: A dense dual-task network for tumor-infiltrating lymphocyte detection and segmentation in histopathological images of breast cancer," *Med. Image Anal.,* vol. 78, no. 5, p. 102415, 2022.
8. S. Singh and R. Kumar, "Breast cancer detection from histopathology images with deep inception and residual blocks," *Multimed. Tools Appl.,* vol. 81, no. 4, pp. 5849–5865, 2022.
9. Y. Zou, J. Zhang, S. Huang, and B. Liu, "Breast cancer histopathological image classification using attention high-order deep network," *Int. J. Imaging Syst. Technol.,* vol. 32, no. 1, pp. 266–279, 2022.
10. S. Ramesh, S. Sasikala, S. Gomathi, V. Geetha, and V. Anbumani, "Segmentation and classification of breast cancer using novel deep learning architecture," *Neural Comput. Appl.,* vol. 34, no. 19, pp. 16533–16545, 2022.
11. N. Ranjan, P. V. Machingal, S. S. D. Jammalmadka, V. Thenaknidiyoor, and A. D. Dileep, "Hierarchical approach for breast cancer histopathology images classification," *OpenReview,* 2022. Available: https://openreview.net/pdf?id=rJlgvtojg [Accessed by 12/10/2024].
12. S. C. Wetstein, V. M. T. de Jong, N. Stathonikos, M. Opdam, G. M. H. E. Dackus, J. P. W. Pluim, P. J. van Diest, and M. Veta, "Deep learning-based breast cancer grading and survival analysis on whole-slide histopathology images," *Scientific Reports,* vol. 12, no. 1, pp. 1–12, 2022.
13. D. Murcia-Gomez, I. Rojas-Valenzuela, and O. Valenzuela, "Impact of image preprocessing methods and deep learning models for classifying histopathological breast cancer images," *Applied Sciences,* vol. 12, no. 22, pp. 1–18, 2022.

14. V. Mohanakurup, S. M. Parambil Gangadharan, P. Goel, D. Verma, S. Alshehri, R. Kashyap, and B. Malakhil, "Breast cancer detection on histopathological images using a composite dilated backbone network," *Comput. Intell. Neurosci.*, vol. 2022, no. 1, pp. 1-10, 2022.
15. F. S. Khan, M. I. Abbasi, M. Khurram, M. N. H. Mohd, and M. D. Khan, "Breast cancer histological images nuclei segmentation and optimised classification with deep learning," *Int. J. Electr. Comput. Eng.*, vol. 12, no. 4, pp. 4099–4110, 2022.
16. A. B. Hamida, M. Devanne, J. Weber, C. Truntzer, V. Derangère, F. Ghiringhelli, and C. Wemmert, "Weakly supervised learning using attention gates for colon cancer histopathological image segmentation," *Artif. Intell. Med.*, vol. 133, no. 11, p. 102407, 2022.
17. D. Addo, S. Zhou, K. Sarpong, O. T. Nartey, M. A. Abdullah, C. C. Ukwuoma, and M. A. Al-Antari, "A hybrid lightweight breast cancer classification framework using the histopathological images," *Biocybern. Biomed. Eng.*, vol. 44, no. 1, pp. 31–54, 2024.
18. M. Amgad, J. M. Hodge, M. A. Elsebaie, C. Bodelon, S. Puvanesarajah, D. A. Gutman, K. P. Siziopikou, J. A. Goldstein, M. M. Gaudet, L. R. Teras, and L. A. D. Cooper, "A population-level digital histologic biomarker for enhanced prognosis of invasive breast cancer," *Nat. Med.*, vol. 30, no. 1, pp. 85–97, 2024.
19. Z. Tabatabaei, A. Colomer, J. O. Moll, and V. Naranjo, "Siamese content-based search engine for a more transparent skin and breast cancer diagnosis through histological imaging," *arXiv preprint arXiv:2401.08272*, 2024. Available: https://arxiv.org/pdf/2401.08272 [Accessed by 18/10/2024].
20. D. Yu, J. Lin, T. Cao, Y. Chen, M. Li, and X. Zhang, "SECS: An effective CNN joint construction strategy for breast cancer histopathological image classification," *J. King Saud Univ.–Comput. Inf. Sci.*, vol. 35, no. 2, pp. 810–820, 2023.
21. P. C. Chhipa, R. Upadhyay, G. G. Pihlgren, R. Saini, S. Uchida, and M. Liwicki, "Magnification prior: A self-supervised method for learning representations on breast cancer histopathological images," *in Proc. IEEE/CVF Winter Conf. Appl. Comput. Vis.*, Hawaii, United States of America, 2023.
22. M. Al-Jabbar, M. Alshahrani, E. M. Senan, and I. A. Ahmed, "Multi-Method Diagnosis of Histopathological Images for Early Detection of Breast Cancer Based on Hybrid and Deep Learning," *Mathematics*, vol. 11, no. 6, pp. 1–24, 2023.
23. S. Majumdar, P. Pramanik, and R. Sarkar, "Gamma function-based ensemble of CNN models for breast cancer detection in histopathology images," *Expert Systems with Applications*, vol. 213, no. 3, p. 119022, 2023.
24. S. Taheri and Z. Golrizkhatami, "Magnification-specific and magnification-independent classification of breast cancer histopathological image using deep learning approaches," *Signal, Image and Video Processing*, vol. 17, no. 9, pp. 583–591, 2023.
25. G. U. Nneji, H. N. Monday, G. T. Mgbejime, V. S. R. Pathapati, S. Nahar, and C. C. Ukwuoma, "Lightweight separable convolution network for breast cancer histopathological identification," *Diagnostics*, vol. 13, no. 2, pp. 1–13, 2023.
26. A. Juhong, B. Li, C.-Y. Yao, C.-W. Yang, D. W. Agnew, Y. L. Lei, X. Huang, W. Piyawattanametha, and Z. Qiu, "Super-resolution and segmentation deep learning for breast cancer histopathology image analysis," *Biomedical Optics Express*, vol. 14, no. 1, pp. 18–36, 2023.
27. Y. Yang, S. Dasmahapatra, and S. Mahmoodi, "ADS_UNet: A nested UNet for histopathology image segmentation," *Expert Systems with Applications*, vol. 226, no. 18, pp. 1–16, 2023.
28. C. Szegedy, S. Ioffe, V. Vanhoucke, and A. A. Alemi, "Inception-v4, inception-resnet and the impact of residual connections on learning," *in Proc. 31st AAAI Conf. Artif. Intell.*, San Francisco, California, United States of America, 2017.
29. R. Rashmi, K. Prasad, and C. B. K. Udupa, "Breast histopathological image analysis using image processing techniques for diagnostic purposes: A methodological review," *Journal of Medical Systems*, vol. 46, no. 1, pp. 1–24, 2022.
30. B. Karthikeyan, R. A. Devi, and M. Munshi, "Utilizing deep learning for the classification of brain tumours using MRI," *AVE Trends in Intelligent Health Letters*, vol. 1, no. 1, pp. 1–9, 2024.
31. S. Vyas, S. Gupta, and M. Chugh, "Metaverse Technologies and Applications: A Study," in Proceedings of the International Conference on Cybersecurity in Emerging Digital Era, *Springer Nature*, Singapore, 2022.
32. U. Obeta, D. Deko, and E. Mantu, "Deep learning-based diagnostic techniques for cancer: Extensive testing and clinical application insights," *AVE Trends in Intelligent Health Letters*, vol. 1, no. 1, pp. 28–37, 2024.
33. M. Chugh, A. Pandey, and S. Vyas, "A Comprehensive Study on the Association Between Personality Traits and Software Development," *in Proceedings of the 4th International Conference on Information Management & Machine Intelligence*, vol. 63, no. 5, pp. 1–6, 2022.
34. M. P. N. V. Kumar, A. Chitra, R. Rajpriya, B. Gayathri, C. Roberts, and S. S. Rajest, "Brain-optimized U-Net model for intraretinal cystoid fluid segmentation in optical coherence tomography," *AVE Trends in Intelligent Health Letters*, vol. 1, no. 1, pp. 38–50, 2024.

35. M. Chugh, S. Gupta, and S. Vyas, “Leveraging the Potentiality of Blockchain Technology for Waste Management in Smart City Development,” in Proceedings of the International Conference on Information and Management Engineering, *Springer Nature*, Singapore, 2022.
36. J. A. Jeba, S. R. Bose, V. K. Kishore, and B. Rehman, “Transforming brain tumor detection via modified detection transformer architectures for enhanced diagnostic outcomes,” *AVE Trends in Intelligent Health Letters*, vol. 1, no. 4, pp. 193–205, 2024.
37. S. Gupta, M. Chugh, and S. Vyas, “A Study on AI-Empowered Smart Healthcare: Key Challenges and Opportunities,” in Proceedings of the International Conference on Smart Systems and Advanced Computing, *Springer Nature*, Switzerland, 2022.